Draft version July 3, 2025
Typeset using LaTeX **twocolumn** style in AASTeX631

The Lockman-SpReSO project. Spectroscopic analysis of Type 1 AGN

Castalia Alenka Negrete [1], Héctor J. Ibarra-Medel [1], Erika Benítez [1], Irene Cruz-González [1], Yair Krongold [1], J.Jesús González,[1] Jordi Cepa,[2,3] Carmen Padilla-Torres,[2,3,4] Miguel Cerviño,[5] Mirjana Povic,[6,7,8] Martín Herrera-Endoqui,[9,1] Nancy Jenaro-Ballesteros,[1] Takamitsu Miyaji,[10] Mauricio Elias-Chávez,[10] Miguel Sánchez-Portal,[11] Bernabé Cedrés,[2] Jacub Nadolny,[2,12] Mauro González-Otero,[13] Bereket Assefa,[6,14] Héctor Hernández-Toledo,[1] J. Antonio de Diego,[1] J. Ignacio González-Serrano,[15] and A. M. Perez Garcia[13,16]

[1] *Instituto de Astronomía, Universidad Nacional Autónoma de México, A.P. 70-264, Ciudad de México, CDMX 04510, Mexico**

[2] *Instituto de Astrofísica de Canarias, E-38205 La Laguna, Tenerife, Spain*

[3] *Departamento de Astrofísica, Universidad de La Laguna (ULL), E-38205 La Laguna, Tenerife, Spain*

[4] *Fundación Galileo Galilei - INAF, Rambla José Ana Fernández Pérez, 7, 38712 Breña Baja, TF - Spain*

[5] *Centro de Astrobiología (CAB, CSIC-INTA), 28692 ESAC Campus, Villanueva de la Cañada, Madrid, Spain*

[6] *Space Science and Geospatial Institute (SSGI), Entoto Observatory and Research Center (EORC), Astronomy and Astrophysics Research Division, PO Box 33679, Addis Abbaba, Ethiopia*

[7] *Instituto de Astrofísica de Andalucía (CSIC), 18080 Granada, Spain*

[8] *Physics Department, Mbarara University of Science and Technology (MUST), Mbarara, Uganda*

[9] *Estancia Posdoctoral por México, CONAHCYT, Coordinación de Apoyos a Becarios e Investigadores*

[10] *Instituto de Astronomía -Ensenada, Universidad Nacional Autónona de México, Km. 107 Carret. Tijuana-Ensenada, Ensenada 22860, Mexico*

[11] *Institut de Radioastronomie Millimétrique, Avenida Divina Pastora, 7, Local 20, E 18012 Granada, Spain*

[12] *Astronomical Observatory Institute, Faculty of Physics and Astronomy, Adam Mickiewicz University, ul. Sloneczna 36, 60-286 Poznań, Poland*

[13] *Asociación Astrofísica para la Promoción de la Investigación, Instrumentación y su Desarrollo, ASPID, 38205 La Laguna, Tenerife, Spain*

[14] *Debre Berhan University, Debre Berhan, Ethiopia*

[15] *Dpto. de Física Moderna, Universidad de Cantabria, IFCA, 39005 Santander (Spain)*

[16] *Centro de Astrobiología (CSIC/INTA), 28692 ESAC Campus, Villanueva de la Cañada, Madrid, (Spain)*

ABSTRACT

We present the first optical-UV spectral systematic analysis of 30 Type 1 AGN selected in the FIR and X-ray in the Lockman-SpReSO Survey. The sample of faint objects (m_B=19.6-21.8) covers a large redshift range of $0.33 > z > 4.97$ with high S/N (∼21 on average). A detailed spectral analysis based on the Quasar Main Sequence phenomenology prescription was applied to deblend the principal optical-UV emitting regions. Our sample span a bolometric luminosity range of $44.85 < \log L_{\rm bol} < 47.87$, absolute B-magnitude -20.46 > M_B > -26.14, BH mass of $7.59 < \log M_{\rm BH} < 9.80$, and Eddington ratio $-1.70 < \log R_{\rm Edd} < 0.56$. The analysis shows that 18 high-z objects correspond to Population B, whereas three low-z fall in Populations A2, B1, and B1+. The remaining eight are candidates to be Pop. B and one Pop. A object. None of them are extreme accretors. We looked for tendencies in our sample and compared them with other samples with different selection criteria. Evidence for winds was explored using CIVλ1549 line half-height centroid $c_{(1/2)}$ finding wind velocities between 941 and -1587 km s^{-1}. This result is consistent with samples with similar ranges of z and M_B. The Baldwin effect showed a slope of -0.23 ± 0.03 dex consistent with previous studies. Spectra from twelve objects in our sample were found in the Sloan Digital Sky Survey Data Release 17 database. We applied the same methodology to compare them to our spectra, finding no evidence of variability.

1. INTRODUCTION

Extragalactic surveys are fundamental building blocks for studying galaxy evolution using data over a wide range of wavelengths. One of the deep fields largely studied is the Lockman Hole (LH). The LH is the best

* SECIHTI Research fellow

Galactic window, well known for having small amounts of neutral hydrogen column density ($N_{\rm H}$). Its central region has a hydrogen column density of $N_{\rm H} = 5.8 \times 10^{19}{\rm cm}^{-2}$ (Lockman et al. 1986; Dickey & Lockman 1990), and has been studied with a wide wavelength coverage (e.g., Fotopoulou et al. 2012; Kondapally et al. 2021; Gonzalez-Otero et al. 2023), making it an ideal region for cosmological studies, particularly in the infrared (IR).

The Lockman Spectroscopic Redshift Survey using OSIRIS (Optical System for Imaging and low-Intermediate-Resolution Integrated Spectroscopy) at the Gran Telescopio Canarias (GTC; Lockman-SpReSO; Gonzalez-Otero et al. 2023, hereafter GO23), is a large Guaranteed Time program that provides deep optical spectroscopy of the far-infrared (FIR) sources from the *Herschel*-PEP survey observed at 100 and 160 μm (Lutz et al. 2011), having optical counterparts in images from OSIRIS in the Sloan Digital Sky Survey (SDSS)-r band.

This survey is intended to complement previous data obtained by space telescopes such as XMM-Newton, Spitzer, and Herschel, as well as radio data. The Lockman-SpReSO (LS) Survey provided a total of 1144 sources in the central $24' \times 24'$region of the LH for a limiting magnitude of $R_C \leq 24.5$ (c.f., Figure 2; GO23); of these, 107 are stellar, and 1037 are extragalactic sources. Details of the characterization of the LS objects are presented in GO23. In particular, the LS Survey aims to establish the principal properties of active and star-forming galaxies in this field and identify new sources using the obtained spectral data.

Within the extragalactic sources, 114 galaxies with nuclear activity have been identified. To achieve a comprehensive study on Active Galactic Nuclei (AGN), it is important to consider the effects of extinction in the spectra when performing those studies. While a dust extinction correction can be applied, it is always assumed based on a dust model. Therefore, it is important to look for places in the galaxy where the transparency is high enough to allow us to obtain observations where the extinction is minimal. In that sense, the LH is the perfect location to perform and study different types of AGN.

For more than three decades, there have been considerable efforts to organize quasars[1] based on their observable properties at different wavelengths (e.g. Boroson & Green 1992; Sulentic et al. 2000b; Shen & Ho 2014). The so-called "Quasar Main Sequence" (QMS; see Panda 2024, for a recent review) has evolved from the four-dimensional Eigenvector 1 (4DE1), which comprises optical data including measurements of virialized components of the central region: the FWHM of the Hβ broad component (H$\beta_{\rm BC}$) and $R_{\rm FeII}$, the ratio of equivalent widths (EW) of FeII (computed in the wavelength range from 4435 to 4685Å) and H$\beta_{\rm BC}$; data in the UV considering the centroid at half intensity $c_{(1/2)}$ of CIVλ1549 as a measure of the contribution of the non-virialized component due to outflows; and the soft X-ray spectral index as a measure of the contribution of ionizing photons that illuminates the BLR. Type 1 AGN have been successfully characterized with the QMS formalism, including high-z objects, as was found recently using the James Webb Space Telescope (JWST) observations (e.g. Loiacono et al. 2024). The QMS finds a dichotomy of Type 1 AGN, dividing them into Population A and B using the FWHM(Hβ) = 4000 km s^{-1}as a boundary. For instance, evidence supporting this division is the change of the Hβ profile from Lorentzian (more adequate to fit Pop. A emission line profiles) to double Gaussian, with a redward asymmetry for Pop. B objects (see Marziani et al. 2018).

This work aims to characterize the Type 1 AGN found in the Lockman-SpReSo survey based on the QMS formalism, and to analyze their properties with other quasar samples at high and low redshifts. A previous study with observations from almost three decades ago reported 43 quasar spectra in the LH (Lehmann et al. 2000, see also Schneider et al. 1998 for a single quasar at z=4.45). Other previous works in the optical range of AGN in the LH field have been focused on its photometric properties (e.g. Rovilos et al. 2011).

In addition, studies using AGN in the Lockman-SpReSo project will be addressed in different papers. For instance, the results obtained from the Type 2 AGN sample will be presented in Assefa et al. (in prep.) along with new identifications of Compton-thick AGN. A multicomponent Spectral Energy Distribution analysis using CIGALE (Boquien et al. 2019) will be presented in Herrera-Endoqui et al. (in prep.). Also, taking advantage of deep XMM-Newton data, X-ray spectral analysis will be given for all sources with sufficient counts within Lockman-SpReSO, including AGN (Elias et al. in prep.).

The paper is organized as follows: Section 2 presents the observations and sample selection. In Section 3, spectral analysis and fitting details are given. Section 4 shows our AGN derived parmeters, and the analysis is presented in 5. In Section 6, a summary listing our main results is provided. Throughout this paper, we

[1] In this work, we use the term quasar and Type 1 AGN equivalently, independent of their luminosity.

use the concordance Cosmology with a Hubble constant $H_0 = 70\,\mathrm{km\,s^{-1}\,Mpc^{-1}}$, $\Omega_m = 0.3$, and $\Omega_\Lambda = 0.7$.

2. LOCKMAN-SPRESO OBSERVATIONS

The details of the Lockman-SpReSO observations are described in Sec. 4 of the survey presentation GO23. In summary, the spectroscopic observations of the faint subset (sources with $20 \leq R_C \leq 24.5$) were carried out using the OSIRIS instrument at the GTC telescope in MOS-mode, hereafter, OSIRIS/GTC. Observations were obtained from 2014 to 2018. The blue region of the spectrum was observed with the R500B grism, which provides a wavelength coverage of 3600-7200 Å and a nominal dispersion of 3.54 Å pixel^{-1}. The red part was covered with two grisms (R500R and R1000R). The former has a wavelength coverage of 4800–10000 Å and a dispersion of 4.88 Å pixel^{-1}, while the latter has a range of 5100–10000 Å and a dispersion of 2.62 Å pixel^{-1}. Table 2 of GO23 provides detailed information about the configuration of the OSIRIS/GTC runs obtained from 2014 to 2018. The data reduction is also described in §5 of GO23. Calibrated 1D spectra were used to obtain redshift estimations and detailed information about each object from the spectral analysis. In this work, we selected the OSIRIS/GTC spectra of a sample of Type 1 AGN identified in the Lockman-SpReSO survey catalog.

2.1. *Sample selection*

From the initial spectroscopic sample of 409 FIR-selected objects from the Lockman-SpReSO catalog, 69 (17%) AGN were identified in González-Otero et al. (2024), hereafter, GO24. The selection criteria are based on X-ray, FIR, and spectroscopic properties, including the use of diagnostic diagrams given by Baldwin et al. (1981). All the AGN spectra were visually inspected to select only those showing broad emission lines (BELs), i.e., only Type 1 with FWHM larger than 1000 km s^{-1}. We obtained a final sample of 30 Type 1 AGN in a large redshift interval of $0.46 < z < 4.97$.

Table 1 contains the list of Type 1 AGN considered in this study. GO23 sub-classified 26 of the Type 1 AGN as X-ray point sources (Xr), 10 as FIR objects, one as a red quasar, and one as a sub-millimetric galaxy (SMG). Six objects have both FIR and Xr classifications. Object 206653 is a BAL (broad absorption line) quasar. All objects were cross-correlated with the SDSS data release 17 (SDSS DR17, Abdurro'uf et al. 2022) database, and 12 objects with spectroscopic observations were identified. The redshift distribution of our sample is presented in Figure 1, where we can see a broad z distribution with a maximum of objects around $z \sim 1.8$, nine objects with $z > 2.4$ and only three low z objects below 0.8. The

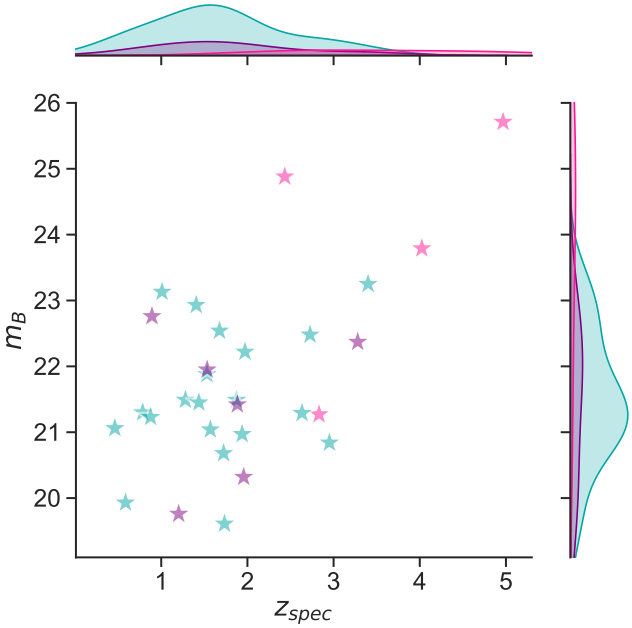

Figure 1. Redshift distribution of Type 1 AGN in the Lockman-SpReSO as a function of the apparent magnitude. The color code corresponds to the Class Identification of GO23: FIR in pink, FIRXr in purple, and Xr in blue.

apparent magnitude in the B band, m_B, is also plotted to show the faintness of our sample. We can see a tendency of the FIR objects towards high-z high-m_B values, while the FIRXr and Xr objects are mixed in a lower-z lower-m_B range.

3. SPECTRAL ANALYSIS

Type 1 AGN provide information on the kinematics of the gas closest to the SMBH. In addition, the diversity of their emission lines, broad permitted and semi-forbidden, and high-, intermediate-, and low-ionization lines allows us to infer the composition and physical properties of the emitting gas. Therefore, careful spectral analysis of each emission line is a fundamental step in optical-UV spectroscopic studies (e.g. Sulentic et al. 2000a; Marziani et al. 2010; Panda 2024). This section defines the main spectral components in the broad and narrow optical and UV spectra to be considered, depending on different kinematic and physical conditions. We also defined the spectral regions selected for our analysis and their spectral components.

3.1. *Methodological considerations*

Spectral analysis of the optical and UV emission lines are performed by separating the virialized broad components (BC) from the wind regions, the narrow lines located in an outer region, the underlying continuum,

ObjID	RA	DEC	z_{spec}	D_L	M_B	GO23	Fitted lines	SDSS DR17
	deg	deg		Mpc	mag	class		
(1)	(2)	(3)	(4)	(5)	(6)	(7)	(8)	(9)
78393	162.83676	57.32841	4.9671	46278	-22.79	FIR	Lyα	
206388	163.15096	57.26719	1.7338	13039	-25.97	FIR	CIV, 1900Å	
206427	163.04043	57.35126	3.2798	28289	-24.89	Xr	Lyα, SiIV, CIV	J105209.70+572104.5
206433	163.18630	57.35626	2.8312	23704	-25.60	Xr	Lyα, SiIV, CIV, 1900Å	J105244.70+572122.4
206445	163.51090	57.37629	1.4058	10069	-22.06	Xr, FIR	1900Å, MgII	
206473	163.51841	57.41341	1.9717	15268	-23.70	FIR	SiIV, CIV, 1900Å	
206475	163.38222	57.41506	1.9564	15123	-25.57	Xr	SiIV, CIV, 1900Å, MgII	J105331.73+572454.0
206479	163.56356	57.41711	4.024	36098	-24.00	Xr	Lyα, CIV	
206482	163.23815	57.41853	1.5309	11186	-23.36	Xr, FIR	1900Å, MgII	J105257.14+572506.8
206489	163.39600	57.42837	0.7848	4901	-22.13	Xr	MgII, Hβ	
206510	163.01541	57.45189	2.4334	19735	-21.60	FIR, red QSO	Lyα, CIV	
206512	163.45927	57.45264	1.7237	12946	-24.88	Xr	CIV, 1900Å, MgII	J105350.22+572709.5
206531	163.28877	57.47232	1.5698	11538	-24.27	Xr, FIR	CIV, 1900Å, MgII	J105309.29+572820.4
206557	163.10252	57.50262	1.009	6681	-20.76	Xr	MgII	
206562	163.24654	57.50832	1.676	12507	-22.95	Xr	CIV, 1900Å	
206570	162.90556	57.51196	0.8922	5739	-20.46	Xr	MgII	
206579	163.41561	57.51794	0.5855	3427	-22.72	Xr	MgII, Hβ, Hγ	
206593	163.05521	57.53933	1.873	14337	-24.30	Xr	CIV, 1900Å	J105213.25+573221.5
206597	163.48816	57.54483	1.28	8967	-23.25	Xr, FIR	1900Å, MgII	J105357.13+573241.4
206623	163.27522	57.57350	2.9514	24922	-26.14	Xr	Lyα, SiIV, CIV, 1900Å	J105306.04+573424.6
206625	162.97661	57.57711	0.877	5619	-22.30	Xr, FIR	MgII	
206641	163.31984	57.59742	1.2023	8298	-24.83	Xr	1900Å, MgII	J105316.76+573550.7
206653	163.51091	57.61362	2.6337	21721	-25.39	Xr	Lyα, SiIV, CIV, 1900Å	
206666	162.90501	57.63184	1.9387	14956	-24.90	Xr, FIR, SMG	SiIV, CIV, 1900Å, MgII	J105137.18+573754.7
206667	163.26008	57.63248	1.8837	14437	-24.38	Xr	SiIV, CIV, 1900Å, MgII	J105302.41+573756.8
206672	163.03078	57.64392	2.7267	22652	-24.30	Xr	Lyα, SiIV, CIV	
206679	163.12537	57.65379	1.437	10345	-23.57	Xr	1900Å	
206692	163.09724	57.68931	1.5326	11201	-23.29	Xr	1900Å, MgII	
206695	163.02548	57.69012	0.4619	2577	-20.94	Xr	MgII, Hβ	
206764	162.93636	57.46886	3.4	29534	-24.10	Xr	Lyα, SiIV, CIV	

Table 1. Type 1 AGN sample. Columns are as follows: (1) object identifier in the catalog by GO23, (2) and (3) RA, DEC (epoch J2000), (4) spectroscopic z_{spec} reported by GO23, (5) luminosity distance in Mpc, (6) absolute magnitude in B band computed from the SDSS photometric system following Jordi et al. (2006), (7) object identification reported by GO23, (8) regions considered for the spectral component fitting, (9) spectra found in the SDSS DR17.

and the FeII pseudo-continuum emission. Our analysis is based on previous works on spectral analysis in the optical (e.g. Zamfir et al. 2010; Negrete et al. 2018; Benítez et al. 2023; Mengistue et al. 2023; Ibarra-Medel et al. 2025) and in the UV ranges (e.g. Marziani et al. 2013a; Negrete et al. 2014; Martínez-Aldama et al. 2018; Garnica et al. 2022; Buendia-Rios et al. 2023), which takes into account the different ionization stages of the broad emitting lines.

Broad lines. BELs are considered to emerge from the virialized BLR. We assume that these emission lines have a symmetric profile characteristic of Doppler broadening. However, we also consider previous studies suggesting that the BLR emission line profiles may be Gaussian or Lorentzian (e.g. Marziani et al. 2010, see also Kollatschny & Zetzl 2013 for analysis of line profile broadening simulations). The choice of the type of profile to use will be constrained by other spectral features, particularly the FWHM, the intensity of the FeII in the optical range, and the CIVλ1549 asymmetry in the UV range. BELs with FWHM $<$ 4000 km s^{-1}, are better fitted with a Lorentzian profile since it describes the central emission and the extended wings characteristic of this profile (see Figure 2 of Marziani et al. 2010, and Figure 2). Usually, these Lorentzian line profiles are accompanied by strong to moderate FeII emission in opti-

cal and UV emission by prominent CIVλ1549 blue asymmetries. For broader lines with FWHM $>$ 4000 km s^{-1}, a Gaussian profile adequately represents the virialized component of the BLR (see Figure 2 in Marziani et al. 2010, and Figure 2). Gaussian profiles are the choice to fit objects with a faint or null FeII optical emission and a more symmetric CIVλ1549 profile. We assume that this broad line is the "core" component of the BLR and should be centered in its respective restframe with a small range of possible shifts within the range of the spectral resolution.

Blue and redshifted line profiles. For the case of intermediate-to-high-ionization lines (IILs and HILs), a blueshifted component associated with outflow winds is expected (Sulentic et al. 2007, 2017). This blue component is prominent in the broad lines with FWHM $<$ 4000 km s^{-1}, specifically in the high ionization lines (HILs) CIVλ1549, HeIIλ1640, and SiIVλ1397 in the UV spectra, and in the narrow lines of [OIII] in the optical spectra. The line profile used to fit for the blue component is an asymmetrical Gaussian profile with FWHM $>$ 6000 km s^{-1}(Proga et al. 2000; Panda et al. 2019; Marziani et al. 2022). For broad lines with FWHM $>$ 4000 km s^{-1}, a very broad redshifted component (VBC) can also be present in all BELs. The origin of this VBC remains unclear (Marziani et al. 2010). Some studies suggest that it can be due to optically thin gas present in quasars with low accretion rates that allows matter to approach the inner edge of the accretion disc, creating a region with gas at very high velocities. This redshifted, VBC emission with FWHM $\sim$10,000 km s^{-1}, can become a very prominent component in some spectra that cannot be attributed to other emitting components (e.g. Benítez et al. 2022; Buendia-Rios et al. 2023).

Iron emission. FeII emission is strong in the optical range, as seen in the composite quasar spectrum of Vanden Berk et al. (2001). This FeII emission generates a pseudo-continuum, extending from 4000 to 5400 Å, and is the product of the multiplet transitions of the ion (e.g. Kovačević et al. 2010; Mengistue et al. 2023). We will consider the optical FeII template used in Negrete et al. (2018) obtained from a high-resolution spectrum of I Zw 1 plus a model of the emission computed by a photoionization code in the Hβ range (see also Marziani et al. 2009). The FeII emission is also blended and strong in the vicinity of MgIIλ2800 (Sameshima et al. 2009; Marziani et al. 2013a; Prince et al. 2023). In the UV range around 2800 Å, we consider Bruhweiler & Verner (2008) FeII emission templates computed from CLOUDY simulations (Ferland et al. 2009). In the range around the 1900 Å blend, FeII is not as intense, and we only consider the emission of FeIIλ1785 (FeIIUV191) as an isolated component. In contrast, the FeIII emission is intense between 1840-2120 Å (Negrete et al. 2012). For the FeIII multiplets, we used the template of Vestergaard & Wilkes (2001).

Narrow lines. All permitted and forbidden narrow emission lines were assumed to be created in the external low-density (log n$_{\rm H}$ $\sim$ 4) narrow line region (NLR). The typical FWHM of these lines is below 1000 km s^{-1}, except for a second blueshifted component of [OIII], which can reach up to 2000 km s^{-1} (the semi-broad SB component Negrete et al. 2018). We assume that all narrow components (NCs) are emitted in the same region and, therefore, share the same kinematics. So, for each fitting range, the same FWHM and offsets were used for all narrow lines in that region.

Continuum. Whenever possible, we fitted a single power-law to account for the underlying continuum of the whole spectral range. We use continuum windows around 1280, 1350, 1450, 1700, 2150, 3000, 4440, and 5100 Å (see e.g. Francis et al. 1991). A special treatment for the continuum was considered in the Lyα range owing to the Lyα forest (Rauch 1998). A series of absorption lines on the blue side of Lyα are expected because of the hydrogen clouds located in our line of sight. To set the continuum under the Lyα range, we assume the continuity of the power-law considering the continuum windows at 1350 Å and 1700 Å.

3.2. *Spectral fitting*

We used the IRAF-SPECFIT task (Kriss 1994) to perform the spectral fitting. SPECFIT simultaneously fits the emission and absorption line components and the continuum models. It requires selecting a set of functional forms to model the emission and absorption line components, the underlying continuum, and the power-law index. Subsequently, SPECFIT fits the strong BELs, followed by the narrow components and FeII optical pseudo-continuum. SPECFIT can use Gaussian or Lorentzian line profiles by inputting their intensity, central wavelength, and FWHM. Therefore, SPECFIT can model complex line systems, such as the complicated continuum of FeII, blended emission lines, and extinction. The fit uses a χ^2 minimization with a Marquardt grid fit algorithm from Numerical Recipes (Press et al. 1986; Kriss 1994).

The considerations set in the previous section allow us to constrain the general parameters of spectral lines. We now describe the spectral features associated with the expected physical conditions for the emission lines, which will help us constrain the number of free parameters in the spectral fits. For each spectral range described below, the most intense line was first fitted, if

more than one emission line was observed within the spectral range. For objects with $z > 2.4$, the most intense line is Lyα, however, this is also the line with the largest absorption. Thus, for objects with $z > 1.28$, the dominant line is CIVλ1549.

Hβ. The spectral range considered was 4440 - 5400 Å. The continuum was fitted considering the windows at 4440 and 5100 Å, followed by the FeII pseudo-continuum. We then model the Hβ BC, the narrow and SB components of [OIII]$\lambda\lambda$4959,5007 considering the theoretical 1:3 ratio (Osterbrock 1981), and the NC of Hβ. Finally, the fit of HeIIλ4687 was included by considering the residuals. For object 206579, the high S/N and spectral coverage allowed the modeling of Hγ to be done together with the fit of Hβ.

MgIIλ2800. The fitted range is from 2600 to 3050 Å. The continuum was fitted considering both the window at 3000 Å and FeII$_{UV}$ emission. MgIIλ2800 is a doublet where we consider a line ratio of I(MgIIλ2796.35)/I(MgIIλ2803.53) = 0.8 (Marziani et al. 2013a,b). Using the Bruhweiler & Verner (2008) FeII template gives us a residual around 2950 Å associated with an emission of FeI, which we fitted with a Gaussian component. Looking at the residuals, a single MgIIλ2800 NC was considered to achieve the best fit for some objects.

1900Å blend. The main emissions in the spectral range between 1750 and 2000 Å are three IILs: CIII]λ1909, SiIII]λ1892, AlIIIλ1860. Of particular importance are the CIII]λ1909 and SiIII]λ1892 lines, as they are broad semi-forbidden lines and have served to constrain the physical parameters in the emitting region, mainly the density and the ionization parameter (Negrete et al. 2012, 2013, 2014; Garnica et al. 2022). The AlIIIλ1860 doublet was fitted using two separate components at 1854.6 and 1862.2 Å and a line ratio 1:1.25. In this region, FeIII emission is also observed, which is particularly intense in objects where AlIIIλ1860 is also intense (see Sections 3.1 and 4). We also expect the contribution of multiplets of FeII as seen in Negrete et al. (2014); however, we fitted only the strongest line FeIIλ1785 as the rest of the lines of the multiplet are much fainter and buried under the blend. Finally, we consider weaker emissions around the blend such as SiIIλ1816 and NIIIλ1750.

CIVλ1549, HeIIλ1640, and SiIVλ1397. As these three lines share high ionization potentials, they were fitted with the same BC profile, FWHM, shift, and several complementary components that share the same profile (see Sec. 3). CIVλ1549 and HeIIλ1640 were fitted at the same time because the blue side of HeIIλ1640 is usually blended with the red wing of CIVλ1549. We model SiIVλ1397 separately because in high-z objects, it lies on the blue edge of the spectra and becomes noisy or with large flux uncertainties. It is well known that the SiIVλ1397 doublet is blended with OIVλ]1402. However, the OIVλ]1402 BC emission is expected to be negligible in comparison to the SiIV emission (Juarez et al. 2009; Negrete et al. 2012, 2014). We fitted the CIVλ1549 line in the range 1450-1700 Å, setting the BC of CIVλ1549 in its restframe, to reach its maximum intensity. Based on the residuals, a blue and/or a rdshift component as described in Sec. 3.1 I is considered. Then we fitted HeIIλ1640 and other faint lines such as OIIλ1304 and NIVλ1684. SiIV: The λ1400 blend was fitted similarly to the CIVλ1549, in the range of 1350-1450 Å, using those found in CIVλ1549as initial conditions. We used a BC considering the doublet with individual lines at 1402 and 1394 Å and a flux ratio $F(1394) = 0.91\ F(1402)$. In agreement with the CIVλ1549 fit, a blue and/or redshifted component was fitted for some objects.

Lyα region. In addition to the Lyα components that were fitted based on the emission components and line profiles of CIVλ1549, we also consider modeling NVλ1240, SIIλ1263, OIIλ1304, and CIIλ1335 lines to obtain a more robust fitting. We used Gaussian profiles to model these extra components, fixing the line shifts and widths of the faintest components to have the same values. The fitting range used is between 1180 and 1350 Å. For objects with absorption produced by the Lyα forest, the range was shortened to 1210-1350 Å, and some absorption lines were fitted using a Gaussian model to recover the broad line.

4. AGN DERIVED PARAMETERS

In this section, we report the line profile parameters of our sample along with the derived parameters obtained from the spectral fitting analysis. Individual parameters like λ_{cent}, f_{line}, FWHM, velocity shifts, EW, measured in the spectral regions described in Sec. 3.2, as well as the individual computations of the derived parameters (L_{bol}, M_{BH}, and R_{Edd}[2]) and the figures showing the fit done in each spectral region, are available by contacting the corresponding author upon request. Figure 2 shows examples of each spectral range covering Lyα, SiIVλ1397, CIVλ1549, 1900 Å blend, MgIIλ2800, and Hβ for Lorentzian and Gaussian broad component profiles.

The SMBH masses (M_{BH}) were estimated using different calibrators compiled from the literature, using virial-

[2] R_{Edd}= L_{bol}/L_{Edd} is the Eddington ratio, the ratio of the bolometric luminosity (L_{bol}) and the Eddington luminosity (L_{Edd} = 1.26 $\times 10^8$ $M/M_\odot$ erg s^{-1}).

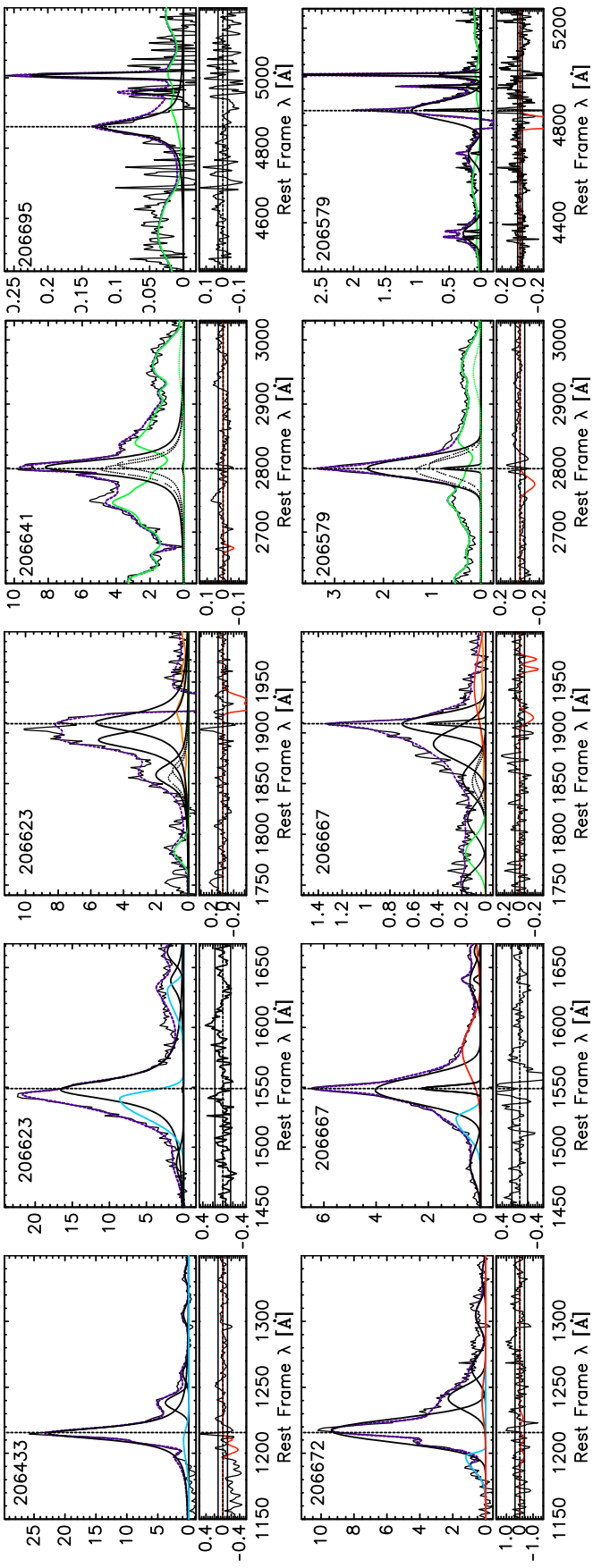

Figure 2. Examples of spectral fitting using Lorentzian (upper panels) and Gaussian (lower panels) profiles for Lyα, CIVλ1549, 1900Å blend, MgIIλ2800, and Hβ. The ordinate is the restframe wavelength, while the abscissa is the flux in units 10^{-16} ergs s^{-1} cm^{-2} Å^{-1}, considering the continuum subtracted. The thin black line represents the observed spectra, thick black lines represent the BC, blueshifted components are in blue, VBC emissions are in red, and narrow lines are in gray. The purple dashed line is the sum of all the fitted components. The vertical dashed line is the restframe. Green continua in MgIIλ2800 and Hβ are the FeII template. In the 1900Å blend, the FeIII template is shown in orange. The lower panels are the residuals, with red lines showing the absorption lines considered in the fit.

Line	Cont(Å)	B.C.	Ref(B.C.)	α	β	Ref(M_{BH})
(1)	(2)	(3)	(4)	(5)	(6)	(7)
Hβ	5100	10.33	R06	0.50	6.91	VP06
MgII	3000	5.15	R06	0.62	6.75	TN12
AlIII	1700	6.3	MS14	0.58	3.24	BR23
CIV	1350	3.5	S17	0.63	3.35	M19

Table 2. Values used for computing the M_{BH} using eq. 1.

ized BC in different regions of the optical-UV spectrum. We compiled the α and β coefficients of the equation

$$\log M_{BH,Line} = \log\left\{\left[\frac{(FWHM\,(Line))}{1000\ km\,s^{-1}}\right]^2\left[\frac{\lambda L_\lambda\,(Cont)}{10^{44}\ ergs\ s^{-1}}\right]^\alpha\right\}+\beta \quad (1)$$

from the works of Vestergaard & Peterson (2006, VP06) for Hβ, Trakhtenbrot & Netzer (2012, TN12) for MgIIλ2800, Buendia-Rios et al. (2023, BR23) for AlIIIλ1860, and Marziani et al. (2019, M19) for CIVλ1549. It is important to note that for the M_{BH} computations considering CIVλ1549, M19 isolate the virialized BC from the wind blueshifted component. Equation 1 computes the M_{BH} using different virial estimators, where λL_λ is the continuum luminosity Cont(Å), in a specific continuum window, and FWHM(line) is from the reference line. Table 2 resumes the values used in eq. 1. The references for the bolometric correction (B.C.) are Sulentic et al. (2017, S17), Marziani & Sulentic (2014, MS14), and Richards et al. (2006, R06). Krawczyk et al. (2013) propose later a BC = 2.75 in the UV at 2500Å, using an integrated spectral energy distribution from 1 μm to 2 keV. However, the difference with R06 is not large.

We also computed the Eddington ratio R_{Edd} values, a fundamental parameter underlying the spectral differences in AGN (Sec. 5.1, see also e.g., Marziani et al. 2001). Table 3 reports the continuum flux values and the derived properties of the sample. For FWHM(BC), $\log L_{bol}$, $\log M_{BH}$, and L_{Edd}, the reported errors include the standard deviation of individual computations. The ranges and median values μ of $\log L_{bol}$ (in erg s^{-1}) are:

- $\log L_{bol,1350}$ = 46.11–47.87, μ = 47.23
- $\log L_{bol,1700}$ = 45.98–47.95, μ = 46.84
- $\log L_{bol,3000}$ = 44.67–47.30, μ = 45.54
- $\log L_{bol,5100}$ = 45.13–45.80, μ = 45.78

In this $\log L_{bol}$ distribution, we see a trend in the increasing $\log L_{bol}$ median values towards the smallest wavelengths, except for $\log L_{bol}$(5100Å). This is because the 5100Å range was obtained from three objects, whereas the 3000Å range from 15 objects spanning a wider L_{bol} range.

Figure 3 presents the dispersion of M_{BH} as a function of $\log L_{bol}$ of the individual virial estimators and individual continuum luminosities. We also show the distribution of M_{BH} in the redshift range and the relationship between R_{Edd} and the FWHM of the BCs. Colored dots are the individual computations for each virial estimator. We used star symbols to highlight the average values. For objects with a single value, the colored dot is superimposed on the star, where the lines connecting the dots to the stars show the values associated with an object. We observed a clear trend in the R_{Edd} vs. FWHM plot and derived the anti-correlation using the FWHM normalized by 1000 km s^{-1}:

$$\log R_{Edd} = -0.17\,\mathrm{FWHM}_{1000}(BC) + 0.27 \quad (2)$$

with a correlation coefficient r_p=-0.7. The correlation described above is expected as the M_{BH} that is used to compute R_{Edd} uses the FWHM values. This expected trend is also shown in the lower panel of Fig. 3. Both relations, expected and derived, are consistent with the sample distribution, within the errors. However, previous works using M_{BH} derived from X-ray data show a similar trend, which means. that the R_{Edd} - FWHM is a statistically true correlation (Marziani et al. 2001)

5. ANALYSIS

The optical-UV spectroscopic analysis based on the QMS formalism allowed us to take advantage of the spectral fitting of the emission lines. Each of these lines provides information about the regions where they are emitted, reflecting the gradient of ionization level from the low to high ionization lines. Numerous studies have developed different correlations using observed and derived parameters, which are described in this section and will serve as the basis for our analysis. We also consider the FIR-Xr nature of the LS sample.

Regarding previous spectral observations in the LH field, Lehmann et al. (2000) reported 43 quasar spectra in the LH observed between 1996-1998; 12 of them coincide with those of our sample. However, comparing their estimations with ours was impossible because the fitting methodology is different, and they do not consider all the emission lines used in our analysis.

5.1. *Lockman-SpReSO Type 1 AGN in the Quasar Main Sequence context*

The QMS in the optical bands has been very useful as it traces accretion-rate-dependent trends. Population A objects show higher accretion rates, lower M_{BH}

ObjID (1)	S/N (2)	Profile (3)	FWHM(BC) (4)	$f(1450)$ (5)	$f(1700)$ (6)	$f(3000)$ (7)	$f(5100)$ (8)	$\log L_{bol}$ (9)	$\log M_{BH}$ (10)	$\log R_{Edd}$ (11)
78393	29	L	2057 ± 261	7.64 ± 1.40				47.87 ± 0.16	9.31 ± 0.31	0.56 ± 0.02
206388	12	L	2833 ± 174	1.63 ± 0.20	1.36 ± 0.13			46.35 ± 0.15	8.41 ± 0.17	-0.07 ± 0.05
206427	18	L	3283 ± 321	3.10 ± 0.46	2.84 ± 0.43			47.32 ± 0.20	9.50 ± 0.22	-0.39 ± 0.16
206433	25	L	3564 ± 240	5.02 ± 0.92	4.18 ± 0.19			47.36 ± 0.18	9.25 ± 0.16	0.08 ± 0.04
206445	37	G	6464 ± 225		3.15 ± 0.14	1.26 ± 0.04		46.49 ± 0.05	9.29 ± 0.07	-0.85 ± 0.09
206473	21	L	3395 ± 497	1.18 ± 0.12	1.11 ± 0.07			46.37 ± 0.12	8.56 ± 0.18	-0.28 ± 0.06
206475	41	G	5635 ± 399	5.37 ± 0.47	5.38 ± 0.25	3.12 ± 0.11		47.12 ± 0.13	9.53 ± 0.12	-0.42 ± 0.06
206479	10	L	2764 ± 229	5.56 ± 0.92	4.63 ± 0.56			47.76 ± 0.20	9.33 ± 0.24	0.20 ± 0.05
206482	16	L	3234 ± 748	2.43 ± 0.31	1.95 ± 0.13	1.33 ± 0.13		46.49 ± 0.12	8.68 ± 0.29	-0.29 ± 0.06
206489	17	G	9546 ± 376			0.87 ± 0.01	0.42 ± 0.03	45.69 ± 0.08	9.25 ± 0.07	-1.70 ± 1.09
206510	6	L	2245 ± 145	0.56 ± 0.10	0.34 ± 0.07			46.18 ± 0.26	8.25 ± 0.26	-0.15 ± 0.11
206512	27	G	5901 ± 414	1.56 ± 0.14	1.12 ± 0.07	0.74 ± 0.07		46.36 ± 0.19	9.13 ± 0.15	-0.85 ± 0.22
206531	31	G	4750 ± 304	3.33 ± 0.23	3.43 ± 0.09	1.88 ± 0.30		46.67 ± 0.21	9.12 ± 0.15	-0.55 ± 0.12
206557	17	G	4296 ± 99			0.57 ± 0.05		45.67 ± 0.07	8.61 ± 0.11	-1.05 ± 0.39
206562	13	G	9483 ± 232	1.17 ± 0.17	0.61 ± 0.05			46.07 ± 0.16	9.32 ± 0.15	-1.30 ± 0.78
206570	12	G	6098 ± 362			0.12 ± 0.01		44.85 ± 0.08	8.40 ± 0.15	-1.70 ± 1.95
206579	37	G	4672 ± 86			2.25 ± 0.08	0.79 ± 0.02	45.73 ± 0.05	8.65 ± 0.05	-1.00 ± 0.13
206593	33	G	11788 ± 281	2.29 ± 0.29	1.91 ± 0.06			46.58 ± 0.12	9.80 ± 0.10	-1.22 ± 0.51
206597	28	G	6621 ± 160			1.00 ± 0.03		46.17 ± 0.03	9.35 ± 0.05	-1.30 ± 0.26
206623	47	L	3570 ± 141	13.21 ± 0.43	11.32 ± 0.28			47.83 ± 0.04	9.60 ± 0.11	0.21 ± 0.01
206625	18	G	4234 ± 90			0.60 ± 0.03		45.54 ± 0.04	8.52 ± 0.06	-1.10 ± 0.22
206641	66	L	2466 ± 99			15.59 ± 0.32		47.30 ± 0.02	9.18 ± 0.06	0.01 ± 0.01
206653	19	G	5821 ± 412	3.92 ± 0.25	3.64 ± 0.13			47.20 ± 0.07	9.49 ± 0.11	-0.35 ± 0.04
206666	29	G	7381 ± 436	3.60 0.16	3.12 ± 0.10			46.82 ± 0.05	9.65 ± 0.07	-0.89 ± 0.10
206667	13	G	5480 ± 763	0.94 ± 0.09	0.55 ± 0.06	0.67 ± 0.08		46.17 ± 0.24	9.02 ± 0.26	-0.85 ± 0.28
206672	15	G	5260 ± 583	1.75 ± 0.11	1.33 ± 0.12			46.84 ± 0.10	9.32 ± 0.18	-0.66 ± 0.12
206679	22	G	5500 ± 277		0.70 ± 0.08			45.98 ± 0.05	8.68 ± 0.16	-0.80 ± 0.16
206692	18	L	3963 ± 176	2.15 ± 0.18	3.16 ± 0.10	1.03 ± 0.25		46.54 ± 0.23	8.90 ± 0.18	-0.40 ± 0.14
206695	13	L	2435 ± 379			0.38 ± 0.01	0.33 ± 0.02	44.90 ± 0.08	7.59 ± 0.18	-0.80 ± 0.14
206764	15	L	2390 ± 128	2.75 ± 0.79				47.16 ± 0.25	9.06 ± 0.33	0.07 ± 0.11

Table 3. Derived parameters. Col. (1) is the object identification. Col. (2) is the largest S/N value around the given continuum window of the following four columns. Col. (3) is the adopted line profile, Col. (4) are the FWHM average values of the BCs in km s^{-1}. Cols. (5-8) is the continuum flux in units 10^{-16} erg^{-1} s^{-1} cm^{-2} $Å^{-1}$. Cols. (9,10) are the average values of the logarithm of the L_{bol} and M_{BH}, and Col. (11) is the average value of the R_{Edd}.

and mostly radio-quiet. A classification in sub-bins has been proposed to group objects with similar spectra and, thus, physical conditions. Populations A1, A2, A3, A4 are defined in terms of increasing FeII emission in bins of $\Delta R_{FeII} = 0.5$. Objects in A3-A4 sub-bins are identified as extreme accretors (xA quasars) in the sense that their accretion rate is close to the Eddington limit. Population B objects have low accretion rates, much higher M_{BH} and are mostly radio-loud quasars. Populations in the sub bins B1, B1+, B1++ are defined in terms of increasing ΔFWHM = 4000 km s^{-1} (Marziani et al. 2010).

In the ultraviolet range, computing the half-height centroid $c_{(1/2)}$ of CIVλ1549 (see section 5.3, eq. 3) is not a straightforward task for large samples, as the line should be cleaned first from the extra emission, mostly the CIVλ1549 narrow component and HeIIλ1640. Therefore, we considered the work of Marziani & Sulentic (2014), who showed that using line ratios in the UV, could be useful to detect highly accreting objects (see also Martínez-Aldama et al. 2018; Garnica et al. 2022; Buendia-Rios et al. 2023, Jenaro-Ballesteros BSc thesis[3]). The UV diagram involves line ratios of the intermediate ionization lines of the 1900 Å blend, CIII]/AlIII, and AlIII/SiIII]. This UV diagram also allows the identification of objects with high (CIII]/AlIII < 1) and low (CIII]/AlIII > 1) accretion rates, as well as xA objects (CIII]/AlIII < 1, and CIII]/AlIII > 0.5).

Using our spectral measurements, we reproduced the optical QMS for the three objects at $z < 0.8$ and compared the results with archival data from Zamfir et al. (2010) and Negrete et al. (2018). The upper panel of Fig. 4 shows the optical QMS with the objects in LS shown as green stars (the three objects are classified as Xr sources). Two belong to Pop. B and one to the Pop. A region. None of them were in the xA domain.

For the UV range, we compiled spectroscopic information from Martínez-Aldama et al. (2018); Sulentic et al.

[3] http://132.248.9.195/ptd2023/octubre/0847307/Index.html

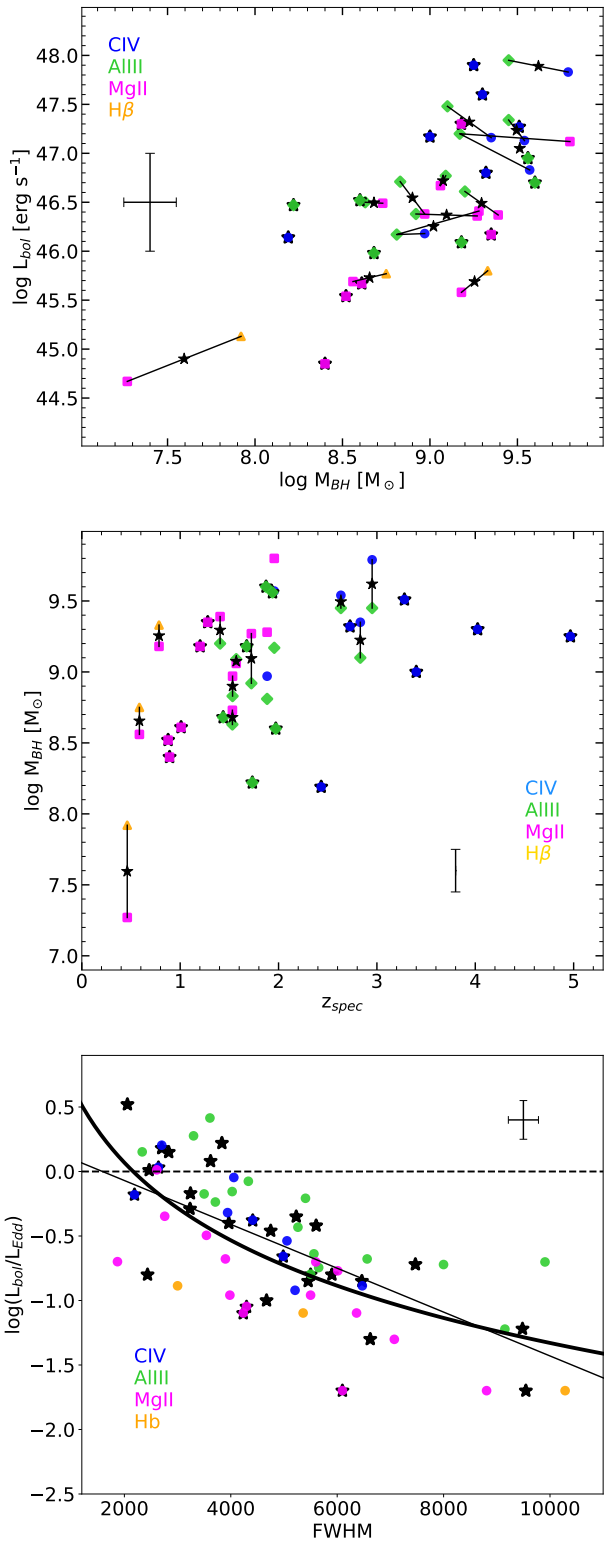

Figure 3. Distributions of $\log M_{BH}$ - $\log L_{bol}$ (*upper panel*), $\log M_{BH}$ in the z range (*middle panel*), and $\log R_{Edd}$ - FWHM(BC) (*lower panel*). In the lower panel, the dashed horizontal line corresponds to $R_{Edd} = 1$, the solid thin line represents an anti-correlation between both quantities, and the solid thick line is the expected correlation of R_{Edd} and the FWHM

. The average error bars are also shown.

(2014); Negrete et al. (2014); Buendia-Rios et al. (2023, 2025 submitted) to build the CIII]λ1909/SiIII]λ1892 vs. AlIIIλ1860/SiIII]λ1892 diagram (shown in middle panel of Fig. 4). In this UV QMS, the 18 LS objects showing the 1900 Å blend fall into Pop. B region, with three objects at the boundary of Pop. A. In this subsample, we have one FIR object that, together with a FIRXr object, falls in the higher part of the CIII]λ1909/SiIII]λ1892 values. Of the remaining nine objects, three have only MgII emission. Taking into account the analysis of Marziani et al. (2013b,a) that uses the FWHM as a tracer of the Population membership, the three objects are Pop. B. The other five objects have CIVλ1549 emission, four with Lorentzian profiles (and then are Pop. A objects) and one with a Gaussian profile (a sign of Pop. B object). Finally, one spectrum has only Lyα emission with Lorentzian profile, so it could be considered a Pop. A object. In summary, we have 25 Pop. B and 5 Pop. A objects.

5.2. *FeII in the UV*

The lower panel of Figure 4, shows the relationship between FeII UV/MgII ratio (R_{MgII}) and R_{Edd} of the 16 objects showing MgII (5 FIRXr and 11 Xr sources). We compare the values of the objects in our sample, whose z-range is between 0.46 and 1.96, with two other samples. The first is from the work of Shin et al. (2021, Sh21, grey circles), who used 29 objects observed by the Hubble Space Telescope (HST) at $z < 0.37$ (with a mean value of 0.04). Sh21 explained the scenario of the close correlation between R_{MgII} and R_{Edd} as a consequence of metal cooling, leading to an increase in the gas inflow and, consequently, the accretion rate. The second sample corresponds to the SDSS DR17 Quasar Catalogue properties of Wu & Shen (2022, shown in color code). From this second sample, we consider spectra with S/N > 5 in the integrated G band, which is the minimum value of our sample, and $\log L_{bol} > 40$, which is a similar range to our sample. In addition, we define a redshift range from $0.53 < z < 2.2$. This range assures that the spectral region of FeII UV and MgII are visible within the SDSS DR17 spectral range. We obtained a selection of 208,000 objects. As reported by Sh21, see their Figure 3, we cannot find a redshift dependency with the R_{MgII} ratio for the SDSS DR17 quasars. However, we find a clear redshift dependency on the R_{MgII}-R_{Edd} relation: the latter decreases as the redshift increases. This implies a trend in the R_{Edd}, where at lower z we find lower values of R_{Edd}, and vice versa, at higher z we have higher values of R_{Edd}. In other words, there is a family of R_{MgII}-R_{Edd} relations dependent on z. When we compare with our sample, the R_{MgII}-R_{Edd} relation is

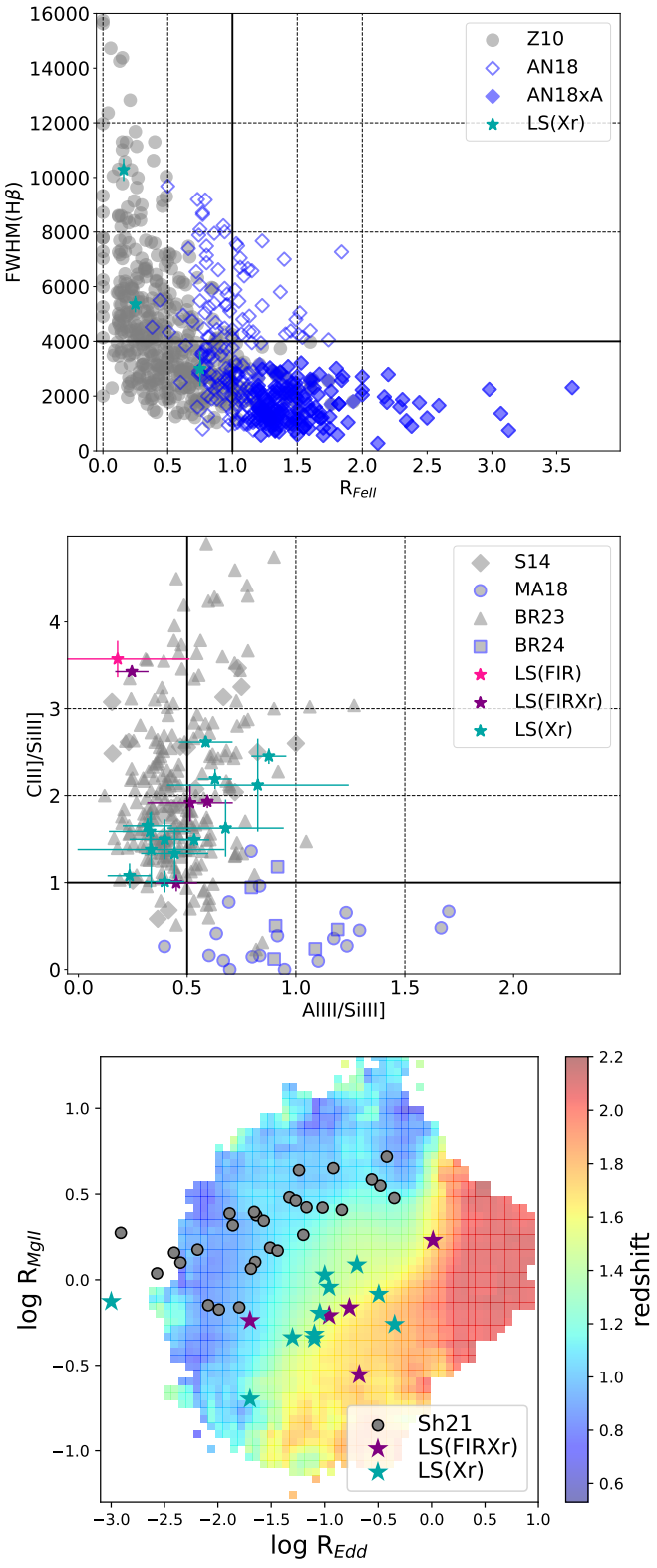

Figure 4. QMS in the optical *(Upper panel)* and UV *Middle panel*. The vertical dashed lines are the boundary for xA objects. The horizontal dashed lines are the boundary separation of Pops. A and B. *Lower panel:* Relation between R_{MgII} and R_{Edd}. The meanings of the symbols are described in the inner boxes. **Grey circles are low z data from Shin et al. (2021), and the color code background is the redshift distribution of the SDSS DR17 sample taken from Wu & Shen (2022).**

in agreement with the SDSS DR17 quasars within our redshift range, showing a clear linear relation between R_{MgII} and R_{Edd}, but with the expected offset from the Sh21 relationship.

5.3. *Winds in the Lockman-SpReSo sample?*

One of the most important properties of Type 1 AGN is the presence of winds arising from the central region, derived by accretion mechanisms (e.g. Elvis 2000). In the BLR, these winds are mainly detected in high-ionization lines, such as CIVλ1549, reaching velocities up to -2500 km s^{-1} (Richards et al. 2011; Wu & Shen 2022). Richards et al. (2011) showed a relationship between the EW and the total shift of the CIVλ1549 line profile, which is argued to be driven by accretion parameters. It is worth noting that the approximation in the works that considers thousands of spectra is based on automatic fits to the emission lines, and the reported blueshift velocities correspond to the total CIVλ1549 emission.

Our approximation considers the QMS formalism, where particular initial conditions were considered for different populations, assuming two different emitting regions. (see Sec. 3.1). The isolated blueshifted CIVλ1549 component has been reported in numerous previous works (e.g. Marziani et al. 2010; Sulentic et al. 2017; Martínez-Aldama et al. 2018, Buendia-Rios et al. 2025 submitted, and references therein).

Another parameter for quantifying the CIVλ1549 blueshift is the half-height centroid c(1/2), defined as

$$c(1/2) = \frac{v_{r,R}(1/2) + v_{r,B}(1/2)}{2} \quad (3)$$

where $v_{r,R}$ y $v_{r,B}$ are the velocity shifts on the red and blue wings at half-height, respectively (Zamfir et al. 2010). Upper panel of Figure 5 shows the distribution of $c_{(1/2)}$ versus FWHM(CIVλ1549) from our sample (LS), compared with samples of Sulentic et al. (2007, hereafter S07) for low z objects, and Sulentic et al. (2014, 2017, hereafter S14, S17) for high z quasars, for faint and bright samples, respectively. In S07 and S17 samples, the tendency to find winds in CIVλ1549 with $c_{(1/2)}$ blueshifts above -4000 km s^{-1} is noticeable. Winds become less prominent in the S14 and LS samples with blueshifts below -1200 km s^{-1}. The LS sample has similar z and logL_{bol} ranges as the S14 and S17 samples. However, the S14 sample was selected considering the flux limits of the LS sample at the highest possible z. On the other hand, the S17 sample was chosen from the Hamburg ESO (HE; Wisotzki et al. 2000) sample as the brightest blue objects at a similar z range to S14. Bluer, brighter quasars at high-z tend to show blueshifts in the

HILs. The middle panel of Figure 5 compares the z-M_B relation from S07, S14, S14, and LS samples, showing that our sample shares a similar M_B magnitude range as the S14 sample, including similar spectral properties. For completeness, we also included the absolute magnitudes from the SDSS DR17 data taken from Wu & Shen (2022, , WS22). In both Figures, we do not find any clear tendency with the FIR-Xr classification, except the one with z mentioned in Sec. 2.1.

Finally, in the optical range, [OIII]$\lambda\lambda$4959,5007 is the HIL that traces these winds (Zamanov et al. 2002; Negrete et al. 2018; Grünwald et al. 2023). Optical winds are identified by the presence of a second semi-broad [OIII]$\lambda\lambda$4959,5007 component shifted to the blue, in addition to the typical narrow component positioned in the restframe. The [OIII] semi-broad wind component can have FWHM up to 2000 km s^{-1} and blueshifts up to -2000 km s^{-1} with respect to the restframe (Negrete et al. 2018). In quasar spectra, semi-broad [OIII]$\lambda\lambda$4959,5007 components with offsets larger than -250 km s^{-1} are considered optical outflows (Zamanov et al. 2002). In our sample, only one object shows a second semi-broad component with an FWHM of 1350 $\pm$ 100 km s^{-1}. It has a shift of -25 $\pm$ 27 km s^{-1}, therefore, it can not be considered a wind component.

5.4. *Baldwin Effect*

The anticorrelation between the EW of CIVλ1549 and the continuum luminosity in high-z UV spectra is known as the Baldwin effect (BE, Baldwin 1977). The BE arises from the relationship between the total line flux over the underlying continuum flux and the underlying continuum luminosity, so the correlation is expected. However, as reported in previous works, the slope of the BE relation is not unity, indicating that the line luminosity does not change by the same amount as the underlying continuum does (e.g., Zheng & Malkan 1993; Wang et al. 2022). The origin of the BE relationship has also been discussed in terms of the Eddington ratio. Bachev et al. (2004, see also Ge et al. 2016) considered UV spectra within the QMS analysis, finding a systematic decrease of the CIVλ1549 EW as the R_{Edd} decreases, suggesting that the origin of the CIVλ1549 BE is the R_{Edd} itself.

The slope on the BE has been reported to be around -0.24 along a wide range of redshifts. For instance, Bian et al. (2012), using the SDSS DR7 with 35000 quasars in a redshift range from 1.5 to 5, obtained a slope of -0.238. The lower panel of Figure 5 shows the BE relation for our sample compared with the high-z samples of S14 and S17. For this analysis, we do not consider the S07 sample as they do not report individual values of the EW(CIVλ1549). As discussed in Section 5.3, our sample

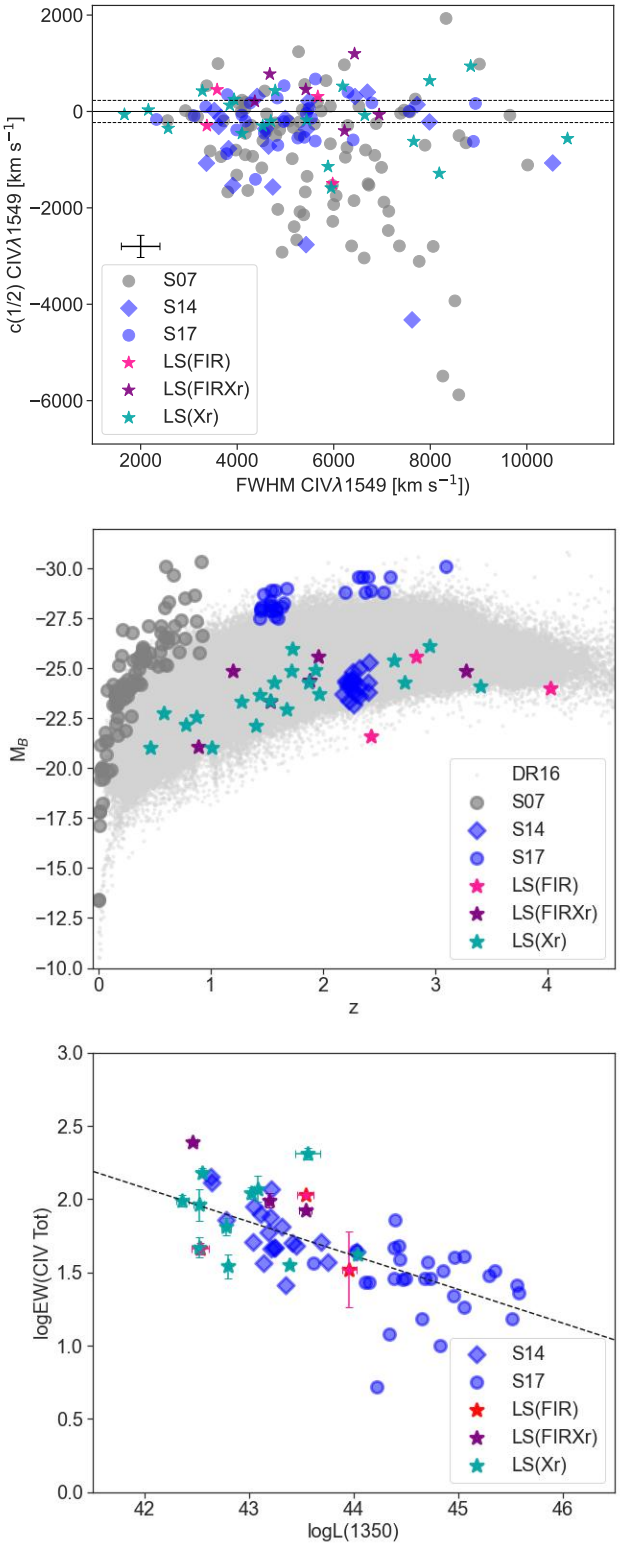

Figure 5. (Upper Panel) Dependence of the velocity shift at half intensity of CIVλ1549, $c_{(1/2)}$ on FWHM(CIVλ1549). The solid line is the reference for zero velocity shift. The dashed lines represent the uncertainty range with respect to zero velocity shift. (Middle Panel) Absolute B-magnitude M_B vs. redshift z. (Lower Panel) Baldwin effect. The dashed line shows the linear fit of our data (Eq. 4). The meanings of the symbols are described in the inner boxes.

shares properties similar to the S14 sample and falls in the same region in the BE diagram. We also do not find any tendency with the FIR-Xr classification. The relationship that we obtain, including S14, S17 and our sample, is:

$$\log EW(CIV) = (-0.23\pm0.03)\log L(1350)+(11.75\pm0.23) \quad (4)$$

with a p-value of -0.67. These values are consistent with the values reported in the literature (e.g. Bian et al. 2012).

5.5. *Comparison with SDSS data*

Given the variable nature of quasars, we searched for the spectra of our sample in the SDSS DR17. We found 10 of these with an observation range between 2014-2016, except for object 206641, which was observed in 2002. The observation range coincides with that of the LS observations (between 2014 and 2018; GO23). The main difference between SDSS and LS data is that the SDSS spectra have higher resolution but lower S/N. Column 9 of Table 1 lists the objects found in SDSS DR17.

We then applied the same criteria and fitting methodology to the spectra observed with our LS sample for the spectral fitting. Then, we look for a one-to-one correlation between the results obtained from the SDSS spectra and our LS sample. It is worth noting that these results can be affected mainly by the low S/N of SDSS spectra. The purpose is to look for evidence of variability that may be due to important changes in the physics of the nuclear region.

The line luminosities correlation (L_{line}, that considers BC line luminosities of Lyα, SiIV, CIV, CIII], AlIII, and MgII) is close to the one-to-one relation with an offset of -0.20±0.24. Therefore, we found a systematic shift between SDSS and LS values of 0.2 dex. However, once the offset error is considered, the SDSS values can be recovered within 1σ of error. In the case of L_{bol} (in the continuum windows 1350 Å, 1700 Å, and 3000 Å) and FWHM of the BCs of Lyα, SiIV, CIV, CIII], AlIII, and MgII) comparisons, the offsets are -0.04 ± 0.28 and -50 ± 820, respectively. Considering the errors, we can conclude that L_{line}, L_{bol}, and the FWHM from the SDSS and LS values are consistent. In addition, we did not find indications of variability between the two samples once scatter was considered.

5.6. *Extinction Analysis*

We examine the effects of extinction in our Galaxy on the flux estimations of quasars. For this purpose, we compare the colors $g_{AB} - r_{AB}$ of our quasar LS sample (located around 57.5° in declination) with other quasar samples taken from the SDSS DR17 in the galactic plane (between ± 15° in declination, group Gal Plane), and the galactic north pole (above 60° in declination, group North Pole). We restrict the three quasar sample to a redshift around z = 1-2 since most of our LS objects are in this range (see Fig. 1). The average color $g_{AB} - r_{AB}$ for the corrected and non-corrected extinction (following the Cardelli et al. 1989, extinction law) of the three groups is:

- LS: 0.233 ± 0.299; dered 0.213 ± 0.276
- Gal Plane: 1.145±0.723; dered 0.200±0.358
- North Pole: 0.195±0.228; dered 0.174±0.227

In conclusion, the current extinction corrections are reliable, especially for objects in the galactic plane, since we can recover the color values.

6. SUMMARY

This paper describes the characteristics of Type 1 AGN identified by the Lockman-SpReSO project. We present high-quality spectra of 30 quasars with a redshift range of 0.462 to 4.967. A detailed spectral fitting method based on the QMS phenomenology prescription was applied to deconvolve the Hβ, MgII, 1900Å blend, CIVλ1549, SiIVλ1397, and Lyα regions found in the spectra of the sample. The overall characteristics of the sample are as follows:

- $\log L_{bol}$: 44.85 – 47.87
- $\log M_{BH}$: 7.59 – 9.80
- $\log R_{Edd}$: −1.70 – 0.56
- M_B: −20.46 – −26.14

The detailed optical-UV spectral splitting allows us to perform different analyses based on correlations of the emission line parameters, properties, and physical conditions of the emission regions reported in previous studies, as described below.

- We found a wide spectral diversity in our sample from the QMS analysis using optical and UV emission lines. The low-z sample (three objects) falls in Populations A2, B1, and B1+, while quasars of the high-z sample, 23 are Pop. B and 4 Pop. A objects. None of the LS quasars was found in the xA domain.
- We reproduced the relationship between the Eddington ratio R_{Edd}, the fundamental parameter underlying the spectral differences in AGN and the FWHM of the virial components, with an

anticorrelation described by log R_{Edd} = -0.17 $FWHM_{1000}$(BC) + 0.27 with a correlation coefficient r_p = -0.7, similar to that reported by Marziani et al. (2001).

- Using the measurements of the spectra showing MgIIλ2800 (in the range $0.462 > z > 1.956$), we recovered the relation R_{Edd}-R_{MgII}, consistent with the results of Shin et al. (2021, for objects with z<0.37) and the SDSS DR17 quasar catalog sample in a z range similar to the LS.

- We also looked for signs of winds in spectra showing the HIL CIVλ1549 in the UV. We computed its half-height centroid $c_{(1/2)}$ as a proxy for the blueshift of the line, finding values of the $c_{(1/2)}$ between 941 and -1587 km s^{-1}. Compared with the other low- and high-z samples of S07, S14, and S17, the LS quasars follow the trends of the S14 sample, which shares a similar range of z and absolute magnitudes.

- We also consider the anti-correlation of the Baldwin effect. We find a trend in terms of log L(1350) vs. log CIV(EW), with a slope of -0.23 $\pm$ 0.03 dex, similar to that reported in the literature, especially by Bian et al. (2012) who used the SDSS DR 16 quasar catalog sample.

- We find 12 spectra of our sample in the SDSS DR17 archive, for which we use the same spectral fitting methodology as with the LS spectra. The principal difference between the SDSS and LS spectra is the low S/N ratio of the former. We found no evidence of spectral variability when comparing values of line luminosities, FWHM, and bolometric luminosities.

- Finally, we perform an extinction analysis comparing the $g_{AB} - r_{AB}$ colors of our sample with an SDSS DR17 quasar sample. The effects of extinction in the LS field are similar to the ones in the Galactic North Pole, while using the extinction law of Cardelli et al. (1989) allows recovery of dereddened colors for objects in the Galactic Plane.

It is worth noticing that despite the LS sample was selected for the large emission in the FIR using Herschel data at 100 and 160 μm, and X-ray data; we found no evidence of different behavior from those AGN in non-obscured or with different criteria selected samples, such as the SDSS.

ACKNOWLEDGEMENTS

CAN and HJIM thank the support of the CONAHCyT projects 2022-320020, CBF2023-2024-1418, and the DGAPA-UNAM grants IA104325 and IN111422. HJIM thanks support from CONAHCyT project CF-2023-G-543. ICG and EB acknowledge financial support from DGAPA-UNAM grant IN-119123 and CONAHCYT grant CF-2023-G-100. MHE acknowledges support from CONAHCYT program Estancias Posdoctorales por México. MC acknowledges funds by grant PID2022-136598NB-C33 funded by MCIN/AEI/10.13039/501100011033 and by "ERDF A way of making Europe". TM, MEC, and MHE thank the support from UNAM DGAPA PAPIIT IN 114423. HMHT acknowledges support from grants CF-G-543 CONAHCYT and CF-2023-G-1052 CONAHCYT. MSP acknowledges the support of the Spanish Ministry of Science, Innovation and Universities through the project PID–2021–122544NB—C43. This work was supported by the Evolution of Galaxies project, of reference PID2021-122544NB-C41 within the Programa estatal de fomento de la investigación científica y técnica de excelencia del Plan Estatal de Investigación Científica y Técnica y de Innovación of the Spanish Ministry of Science and Innovation/State Agency of Research MCIN/AEI. This article is based on observations made with the Gran Telescopio Canarias at Roque de los Muchachos Observatory on the island of La Palma. Funding for the Sloan Digital Sky Survey IV has been provided by the Alfred P. Sloan Foundation, the Heising-Simons Foundation, the National Science Foundation, and the Participating Institutions. SDSS acknowledges support and resources from the Center for High-Performance Computing at the University of Utah. SDSS telescopes are located at Apache Point Observatory, funded by the Astrophysical Research Consortium and operated by New Mexico State University, and at Las Campanas Observatory, operated by the Carnegie Institution for Science. The SDSS web site is www.sdss.org. SDSS is managed by the Astrophysical Research Consortium for the Participating Institutions of the SDSS Collaboration, including Caltech, The Carnegie Institution for Science, Chilean National Time Allocation Committee (CNTAC) ratified researchers, The Flatiron Institute, the Gotham Participation Group, Harvard University, Heidelberg University, The Johns Hopkins University, L'Ecole polytechnique fédérale de Lausanne (EPFL), Leibniz-Institut für Astrophysik Potsdam (AIP), Max-Planck-Institut für Astronomie (MPIA Heidelberg), Max-Planck-Institut für Extraterrestrische Physik (MPE), Nanjing University, National Astronomical Observatories of China (NAOC),

New Mexico State University, The Ohio State University, Pennsylvania State University, Smithsonian Astrophysical Observatory, Space Telescope Science Institute (STScI), the Stellar Astrophysics Participation Group, Universidad Nacional Autónoma de México, University of Arizona, University of Colorado Boulder, University of Illinois at Urbana-Champaign, University of Toronto, University of Utah, University of Virginia, Yale University, and Yunnan University.

REFERENCES

Abdurro'uf, Accetta, K., Aerts, C., et al. 2022, ApJS, 259, 35, doi: 10.3847/1538-4365/ac4414

Bachev, R., Marziani, P., Sulentic, J. W., et al. 2004, ApJ, 617, 171, doi: 10.1086/425210

Baldwin, J. A. 1977, ApJ, 214, 679, doi: 10.1086/155294

Baldwin, J. A., Phillips, M. M., & Terlevich, R. 1981, PASP, 93, 5, doi: 10.1086/130766

Benítez, E., Ibarra-Medel, H., Negrete, C. A., et al. 2023, ApJ, 952, 45, doi: 10.3847/1538-4357/acce3e

Benítez, E., Jiménez-Bailón, E., Negrete, C. A., et al. 2022, MNRAS, 516, 5270, doi: 10.1093/mnras/stac2244

Bian, W.-H., Fang, L.-L., Huang, K.-L., & Wang, J.-M. 2012, MNRAS, 427, 2881, doi: 10.1111/j.1365-2966.2012.22123.x

Boquien, M., Burgarella, D., Roehlly, Y., et al. 2019, A&A, 622, A103, doi: 10.1051/0004-6361/201834156

Boroson, T. A., & Green, R. F. 1992, ApJS, 80, 109, doi: 10.1086/191661

Bruhweiler, F., & Verner, E. 2008, ApJ, 675, 83, doi: 10.1086/525557

Buendia-Rios, T. M., Negrete, C. A., Marziani, P., & Dultzin, D. 2023, A&A, 669, A135, doi: 10.1051/0004-6361/202244177

Cardelli, J. A., Clayton, G. C., & Mathis, J. S. 1989, ApJ, 345, 245, doi: 10.1086/167900

Dickey, J. M., & Lockman, F. J. 1990, ARA&A, 28, 215, doi: 10.1146/annurev.aa.28.090190.001243

Elvis, M. 2000, ApJ, 545, 63, doi: 10.1086/317778

Ferland, G. J., Hu, C., Wang, J., et al. 2009, ApJL, 707, L82, doi: 10.1088/0004-637X/707/1/L82

Fotopoulou, S., Salvato, M., Hasinger, G., et al. 2012, ApJS, 198, 1, doi: 10.1088/0067-0049/198/1/1

Francis, P. J., Hewett, P. C., Foltz, C. B., et al. 1991, ApJ, 373, 465, doi: 10.1086/170066

Garnica, K., Negrete, C. A., Marziani, P., et al. 2022, A&A, 667, A105, doi: 10.1051/0004-6361/202142837

Ge, X., Bian, W.-H., Jiang, X.-L., Liu, W.-S., & Wang, X.-F. 2016, MNRAS, 462, 966, doi: 10.1093/mnras/stw1605

Gonzalez-Otero, M., Padilla-Torres, C. P., Cepa, J., et al. 2023, A&A, 669, A85, doi: 10.1051/0004-6361/202244480

González-Otero, M., Cepa, J., Padilla-Torres, C. P., et al. 2024, A&A, 687, A19, doi: 10.1051/0004-6361/202449238

Grünwald, G., Boller, T., Rakshit, S., et al. 2023, A&A, 669, A37, doi: 10.1051/0004-6361/202244620

Ibarra-Medel, H., Negrete, C. A., Lacerna, I., et al. 2025, MNRAS, 536, 752, doi: 10.1093/mnras/stae2623

Jordi, K., Grebel, E. K., & Ammon, K. 2006, A&A, 460, 339, doi: 10.1051/0004-6361:20066082

Juarez, Y., Maiolino, R., Mujica, R., et al. 2009, A&A, 494, L25, doi: 10.1051/0004-6361:200811415

Kollatschny, W., & Zetzl, M. 2013, A&A, 549, A100, doi: 10.1051/0004-6361/201219411

Kondapally, R., Best, P. N., Hardcastle, M. J., et al. 2021, A&A, 648, A3, doi: 10.1051/0004-6361/202038813

Kovačević, J., Popović, L. Č., & Dimitrijević, M. S. 2010, ApJS, 189, 15, doi: 10.1088/0067-0049/189/1/15

Krawczyk, C. M., Richards, G. T., Mehta, S. S., et al. 2013, ApJS, 206, 4, doi: 10.1088/0067-0049/206/1/4

Kriss, G. 1994, in Astronomical Society of the Pacific Conference Series, Vol. 61, Astronomical Data Analysis Software and Systems III, ed. D. R. Crabtree, R. J. Hanisch, & J. Barnes, 437

Lehmann, I., Hasinger, G., Schmidt, M., et al. 2000, A&A, 354, 35, doi: 10.48550/arXiv.astro-ph/9911484

Lockman, F. J., Jahoda, K., & McCammon, D. 1986, ApJ, 302, 432, doi: 10.1086/164002

Loiacono, F., Decarli, R., Mignoli, M., et al. 2024, A&A, 685, A121, doi: 10.1051/0004-6361/202348535

Lutz, D., Poglitsch, A., Altieri, B., et al. 2011, A&A, 532, A90, doi: 10.1051/0004-6361/201117107

Martínez-Aldama, M. L., Del Olmo, A., Marziani, P., et al. 2018, Frontiers in Astronomy and Space Sciences, 4, 65, doi: 10.3389/fspas.2017.00065

Marziani, P., & Sulentic, J. W. 2014, MNRAS, 442, 1211, doi: 10.1093/mnras/stu951

Marziani, P., Sulentic, J. W., Negrete, C. A., et al. 2010, MNRAS, 409, 1033, doi: 10.1111/j.1365-2966.2010.17357.x

Marziani, P., Sulentic, J. W., Plauchu-Frayn, I., & del Olmo, A. 2013a, ApJ, 764, 150, doi: 10.1088/0004-637X/764/2/150

—. 2013b, A&A, 555, A89, doi: 10.1051/0004-6361/201321374
Marziani, P., Sulentic, J. W., Stirpe, G. M., Zamfir, S., & Calvani, M. 2009, A&A, 495, 83, doi: 10.1051/0004-6361:200810764
Marziani, P., Sulentic, J. W., Zwitter, T., Dultzin-Hacyan, D., & Calvani, M. 2001, ApJ, 558, 553, doi: 10.1086/322286
Marziani, P., Dultzin, D., Sulentic, J. W., et al. 2018, Frontiers in Astronomy and Space Sciences, 5, 6, doi: 10.3389/fspas.2018.00006
Marziani, P., del Olmo, A., Martínez-Carballo, M. A., et al. 2019, A&A, 627, A88, doi: 10.1051/0004-6361/201935265
Marziani, P., Bon, E., Bon, N., et al. 2022, Astronomische Nachrichten, 343, e210082, doi: 10.1002/asna.20210082
Mengistue, S. T., Del Olmo, A., Marziani, P., et al. 2023, MNRAS, 525, 4474, doi: 10.1093/mnras/stad2467
Negrete, C. A., Dultzin, D., Marziani, P., & Sulentic, J. W. 2012, ApJ, 757, 62, doi: 10.1088/0004-637X/757/1/62
—. 2013, ApJ, 771, 31, doi: 10.1088/0004-637X/771/1/31
—. 2014, ApJ, 794, 95, doi: 10.1088/0004-637X/794/1/95
Negrete, C. A., Dultzin, D., Marziani, P., et al. 2018, A&A, 620, A118, doi: 10.1051/0004-6361/201833285
Osterbrock, D. E. 1981, ApJ, 249, 462, doi: 10.1086/159306
Panda, S. 2024, Frontiers in Astronomy and Space Sciences, doi: 10.3389/fspas.2024.1479874
Panda, S., Martínez-Aldama, M. L., & Zajaček, M. 2019, Frontiers in Astronomy and Space Sciences, 6, 75, doi: 10.3389/fspas.2019.00075
Press, W. H., Flannery, B. P., & Teukolsky, S. A. 1986, Numerical recipes. The art of scientific computing (Cambridege University Press)
Prince, R., Zajaček, M., Panda, S., et al. 2023, A&A, 678, A189, doi: 10.1051/0004-6361/202346738
Proga, D., Stone, J. M., & Kallman, T. R. 2000, ApJ, 543, 686, doi: 10.1086/317154
Rauch, M. 1998, ARA&A, 36, 267, doi: 10.1146/annurev.astro.36.1.267
Richards, G. T., Strauss, M. A., Fan, X., et al. 2006, AJ, 131, 2766, doi: 10.1086/503559
Richards, G. T., Kruczek, N. E., Gallagher, S. C., et al. 2011, AJ, 141, 167, doi: 10.1088/0004-6256/141/5/167
Rovilos, E., Fotopoulou, S., Salvato, M., et al. 2011, A&A, 529, A135, doi: 10.1051/0004-6361/201015763
Sameshima, H., Maza, J., Matsuoka, Y., et al. 2009, MNRAS, 395, 1087, doi: 10.1111/j.1365-2966.2009.14605.x
Schneider, D. P., Schmidt, M., Hasinger, G., et al. 1998, AJ, 115, 1230, doi: 10.1086/300307
Shen, Y., & Ho, L. C. 2014, Nature, 513, 210, doi: 10.1038/nature13712
Shin, J., Woo, J.-H., Nagao, T., Kim, M., & Bahk, H. 2021, ApJ, 917, 107, doi: 10.3847/1538-4357/ac0adf
Sulentic, J. W., Bachev, R., Marziani, P., Negrete, C. A., & Dultzin, D. 2007, ApJ, 666, 757, doi: 10.1086/519916
Sulentic, J. W., Marziani, P., del Olmo, A., et al. 2014, A&A, 570, A96, doi: 10.1051/0004-6361/201423975
Sulentic, J. W., Marziani, P., & Dultzin-Hacyan, D. 2000a, ARA&A, 38, 521, doi: 10.1146/annurev.astro.38.1.521
Sulentic, J. W., Zwitter, T., Marziani, P., & Dultzin-Hacyan, D. 2000b, ApJL, 536, L5, doi: 10.1086/312717
Sulentic, J. W., del Olmo, A., Marziani, P., et al. 2017, A&A, 608, A122, doi: 10.1051/0004-6361/201630309
Trakhtenbrot, B., & Netzer, H. 2012, MNRAS, 427, 3081, doi: 10.1111/j.1365-2966.2012.22056.x
Vanden Berk, D. E., Richards, G. T., Bauer, A., et al. 2001, AJ, 122, 549, doi: 10.1086/321167
Vestergaard, M., & Peterson, B. M. 2006, ApJ, 641, 689, doi: 10.1086/500572
Vestergaard, M., & Wilkes, B. J. 2001, ApJS, 134, 1, doi: 10.1086/320357
Wang, Y., Liu, W., Shang, Z., & Brotherton, M. S. 2022, MNRAS, 515, 5836, doi: 10.1093/mnras/stac2076
Wisotzki, L., Christlieb, N., Bade, N., et al. 2000, A&A, 358, 77, doi: 10.48550/arXiv.astro-ph/0004162
Wu, Q., & Shen, Y. 2022, ApJS, 263, 42, doi: 10.3847/1538-4365/ac9ead
Zamanov, R., Marziani, P., Sulentic, J. W., et al. 2002, ApJL, 576, L9, doi: 10.1086/342783
Zamfir, S., Sulentic, J. W., Marziani, P., & Dultzin, D. 2010, MNRAS, 403, 1759, doi: 10.1111/j.1365-2966.2009.16236.x
Zheng, W., & Malkan, M. A. 1993, ApJ, 415, 517, doi: 10.1086/173182